Quenched Pair Breaking by Interlayer Correlations as a Key to Superconductivity in $La_3Ni_2O_7$

Siheon Ryee,[1,*] Niklas Witt,[1,2] and Tim O. Wehling[1,2]
[1]I. Institute of Theoretical Physics, University of Hamburg, Notkestrasse 9, 22607 Hamburg, Germany
[2]The Hamburg Centre for Ultrafast Imaging, Luruper Chaussee 149, 22761 Hamburg, Germany

(Received 13 November 2023; revised 5 June 2024; accepted 29 July 2024; published 30 August 2024)

The recent discovery of superconductivity in $La_3Ni_2O_7$ with $T_c \simeq 80$ K under high pressure opens up a new route to high-T_c superconductivity. This material realizes a bilayer square lattice model featuring a strong interlayer hybridization unlike many unconventional superconductors. A key question in this regard concerns how electronic correlations driven by the interlayer hybridization affect the low-energy electronic structure and the concomitant superconductivity. Here, we demonstrate using a cluster dynamical mean-field theory that the interlayer electronic correlations (IECs) induce a Lifshitz transition resulting in a change of Fermi surface topology. By solving an appropriate gap equation, we further show that the leading pairing instability, $s\pm$ wave, is enhanced by the IECs. The underlying mechanism is the quenching of a strong ferromagnetic channel, resulting from the Lifshitz transition driven by the IECs. Based on this picture, we provide a possible reason of why superconductivity emerges only under high pressure.

DOI: 10.1103/PhysRevLett.133.096002

The recent discovery of superconductivity in bilayer nickelate $La_3Ni_2O_7$ under high pressure [Fig. 1(a)] heralds a new class of high-T_c superconductors [1]. Without doping, this material exhibits superconductivity under pressure exceeding 14 GPa with maximal critical temperature of $T_c \simeq 80$ K [1–5]. A notable feature in $La_3Ni_2O_7$ is a multiorbital nature of low-lying states already at the level of density functional theory (DFT) [1,6–20] [Fig. 1(b)]. Namely, three electrons per unit cell are distributed over Ni-e_g orbitals in the top and bottom square-planar lattices, whereas Ni-t_{2g} orbitals are fully occupied, thereby inactive for the low-energy physics. The two layers are coupled dominantly via interlayer nearest-neighbor hopping (or hybridization) between Ni-d_{z^2} orbitals ($t_\perp^z \simeq -0.63$ eV) [6,8,13]. The hopping between Ni-$d_{x^2-y^2}$ is much smaller ($|t_\perp^x| < 0.05$ eV) [6,8]. Most importantly, $t_\perp^z$ is deemed to be crucial for the noninteracting Fermi surface (FS) topology and theories of superconductivity in $La_3Ni_2O_7$ [12,13,16,18,19,21–29].

In this respect, an important open question concerns how interlayer electronic correlations (IECs) driven by $t_\perp^{x/z}$ modify the low-energy electronic structure and how they affect superconductivity. Since $t_\perp^z$ is the largest among all the hopping amplitudes [6,8], one can identify the interlayer nearest-neighbor electronic correlations in the Ni-d_{z^2} states as the leading "nonlocal" correlations.

In this Letter, we employ a cluster (cellular) dynamical mean-field theory (CDMFT) [31–33] to address nonperturbatively the nonlocal as well as the local electronic correlations within the two-site clusters (dimers) of the bilayer square lattice model for $La_3Ni_2O_7$ [Fig. 1(a)]. One of the key findings of our study is a Lifshitz transition resulting in a change of the FS topology which does not occur when only local correlations are taken into account.

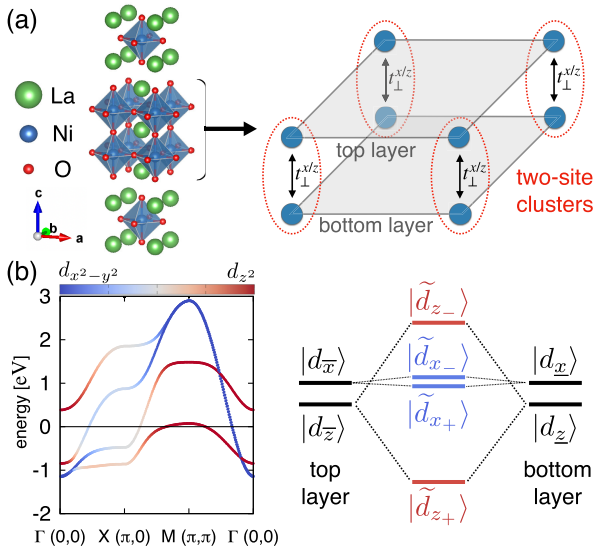

FIG. 1. (a) Left: Crystal structure of $La_3Ni_2O_7$ under high pressure drawn using VESTA [30]. Right: The bilayer square lattice model for $La_3Ni_2O_7$. Dimers consisting of top and bottom layer Ni sites (blue circles) coupled via $t_\perp^{x/z}$ are highlighted with red-dotted ovals. (b) Left: MLWF bands of the DFT electronic structure. The color bar indicates the orbital character. Right: Sketch of the formation of four BA orbitals within the dimer consisting of the Ni-e_g orbitals in the top and bottom layers.

*Contact author: sryee@physnet.uni-hamburg.de

By solving an appropriate gap equation, we show that the IECs promote $s\pm$-wave pairing. The underlying mechanism is the quenching of ferromagnetic (FM) fluctuations resulting from the Lifshitz transition due to IECs. Based on this picture, we provide a possible reason of why superconductivity emerges only under high pressure.

We consider a Hamiltonian on the bilayer square lattice: $\mathcal{H} = H_0 + H_{\rm int}$. Here, H_0 is a tight-binding term for the Ni-e_g subspace describing the band structure for which we use the maximally localized Wannier function (MLWF) description for the DFT result of $La_3Ni_2O_7$ under high pressure (29.5 GPa) [8] [Fig. 1(b)]. $H_{\rm int}$ is the local interaction term between Ni-e_g orbital electrons on the same Ni site, and is given by the standard Kanamori form consisting of U (intraorbital Coulomb interaction), J (Hund's coupling), and U' (interorbital Coulomb interaction; $U' = U - 2J$). We use $U = 3.7$, $J = 0.6$, and $U' = 2.5$ eV by taking *ab initio* estimates for the e_g MLWF model [34]. See Supplemental Material for more information [35].

The impurity problem is solved using the hybridization-expansion continuous-time quantum Monte Carlo method [36,70]. We investigate the system at a temperature of $T = 1/145$ eV $\simeq 80$ K corresponding to the maximum experimental T_c [1]. To mitigate the Monte Carlo sign problem resulting from the large interlayer hybridization in CDMFT, we solve the model in a bonding–antibonding (BA) basis defined as the $+$ or $-$ combinations of the top and bottom layer e_g orbitals:

$$|\tilde{d}_{i\eta_\pm\sigma}\rangle = (|d_{i\bar{\eta}\sigma}\rangle \pm |d_{i\underline{\eta}\sigma}\rangle)/\sqrt{2}. \tag{1}$$

Here, ket symbols indicate the corresponding Wannier states with site index i for the bilayer square lattice and spin $\sigma \in \{\uparrow, \downarrow\}$. $\bar{\eta}$ and $\underline{\eta}$ represent Ni-e_g orbitals ($\eta \in \{x^2 - y^2, z^2\}$) in the top and bottom layers, respectively. Hereafter $x^2 - y^2$ is denoted by x and z^2 by z. Site and spin indices are omitted unless needed. In this BA basis the CDMFT self-energy becomes orbital diagonal and momentum independent, so our CDMFT is equivalent to "four-orbital single-site DMFT." The interlayer hopping $t_\perp^\eta$ between e_g orbitals $|d_{\bar{\eta}}\rangle$ and $|d_{\underline{\eta}}\rangle$ turns into a hybridization gap of $2|t_\perp^\eta|$ between BA orbitals $|\tilde{d}_{\eta_+}\rangle$ and $|\tilde{d}_{\eta_-}\rangle$. Thus a small (large) splitting is realized for $\eta = x$ ($\eta = z$) [schematically shown in the right panel of Fig. 1(b)].

We first investigate how interlayer correlations affect the low-energy electronic structure by contrasting DMFT (in which all the interlayer correlations are neglected [71]) and CDMFT results for the same model. Note that, in a reasonable range around the *ab initio* interaction parameters, neither a Mott transition nor a bad metal behavior emerges within our calculations [35], which is in line with experiments [1–4].

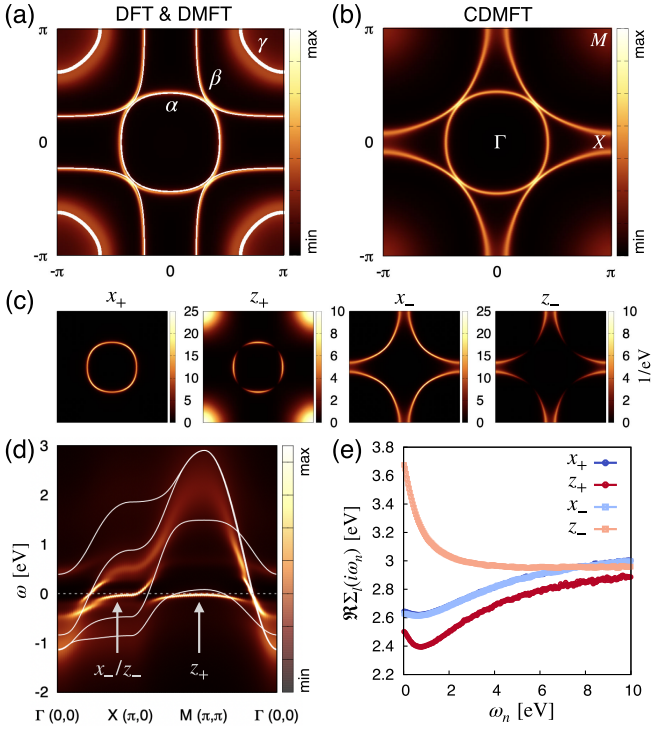

FIG. 2. (a) FSs obtained from the MLWF model of the DFT band structure (white lines) and DMFT (color map). (b) FS from CDMFT. The FSs of DMFT and CDMFT in (a) and (b) are approximated via $-\sum_{lm}\delta_{lm}\Im G_{lm}(\boldsymbol{k}, i\omega_0)$, where $l, m \in \{x_+, z_+, x_-, z_-\}$. (c) The orbital character of the CDMFT FS. (d) The momentum-dependent spectral function obtained from CDMFT using the maximum entropy method [72,73] (color map). The white solid lines indicate the DFT bands. The Fermi level is at $\omega = 0$. (e) The real part of the CDMFT self-energy on the Matsubara frequency axis.

Figure 2 presents the FSs obtained within DMFT and CDMFT. We find from DMFT that the local correlations alone do not affect the FS topology [Fig. 2(a)]. The size and the shape of three FS pockets obtained from DFT, namely α, β, and γ pockets, remain intact. This result is consistent with previous DFT + DMFT studies [7,9,24].

The IECs, however, significantly modify this picture [Fig. 2(b)]. While the α pocket remains nearly unchanged, the β and the γ pockets are largely affected by IECs. The β pocket becomes more diamond shaped with spectral weight at the first Brillouin zone (FBZ) boundary being shifted toward the X point. We also find redistribution of electron occupations in favor of half-filled $\bar{z}$ and $\underline{z}$ orbitals with $\langle n_{\bar{z}}\rangle = \langle n_{\underline{z}}\rangle \simeq 0.93$ compared to the DMFT value of 0.85. Most interestingly, the γ pocket disappears which results in a Lifshitz transition of the FS. Looking at the orbital character of the FS [Fig. 2(c)] reveals that x_- and z_- (for the β pocket around X point) and z_+ (for the γ pocket around the M point) BA orbitals underlie the FS modification.

More information can be obtained from the momentum-dependent CDMFT spectral function [Fig. 2(d)]. Near the

X point, the second lowest band moves upward such that x_- and z_- states get closer to the Fermi level. The flat z_+ character at the M point, on the other hand, sinks below the Fermi level, leading to the disappearance of the γ pocket.

To further pinpoint the microscopic role of IECs, we investigate the CDMFT self-energy $\Sigma_l(i\omega_n)$, where $\omega_n = (2n+1)\pi/T$ is the fermionic Matsubara frequency with n being integer and $l \in \{x_+, z_+, x_-, z_-\}$. Without IECs, $\Sigma_{x_+/z_+}(i\omega_n) = \Sigma_{x_-/z_-}(i\omega_n)$, so IECs are manifested by a difference of the self-energies between the BA orbitals. We first find that $\Sigma_{x_+}(i\omega_n) \simeq \Sigma_{x_-}(i\omega_n)$ over the entire frequency range due to small $t_\perp^x$ resulting in negligible IECs.

In contrast to the $x_\pm$ components, large $t_\perp^z$ gives rise to strong IECs in the $z_\pm$ components. We investigate the real part $\Re\Sigma_l(i\omega_n)$ which modifies the on-site energy level of the orbital l; see Fig. 2(e). See Supplemental Material for the imaginary part [35]. We note first that the Hartree-Fock self-energy, $\Re\Sigma_l(i\omega_\infty)$, does not modify the FS topology because $\Re\Sigma_{x_\pm}(i\omega_\infty) - \Re\Sigma_{z_\pm}(i\omega_\infty)$ is only about 0.1 eV and $\Re\Sigma_{x_+/z_+}(i\omega_\infty) = \Re\Sigma_{x_-/z_-}(i\omega_\infty)$.

In a low-frequency regime ($\omega_n \ll 10$ eV), however, $\Re\Sigma_{z_+}(i\omega_n)$ is smaller and $\Re\Sigma_{z_-}(i\omega_n)$ is larger than the value at infinite frequency. This, in turn, shifts effectively the onsite energy levels of $z_\pm$ upward (z_-) and downward (z_+) with respect to their DFT counterparts, thereby enhancing the hybridization gap. In fact, this low-energy behavior is the origin of the shifts of spectral weight and concomitant FS change seen in Fig. 2(b). Near the X point z_- has substantial weight in the β pocket of the noninteracting FS. Thus the large upturn of $\Re\Sigma_{z_-}(i\omega_n)$ as $\omega_n \to 0$ makes an upward shift in energy near the X point, leading to the change of the β pocket in CDMFT; see also Supplemental Material [35]. The physics here bears a close resemblance to that of VO_2 in which intersite correlations within dimers promote intradimer singlets with an enhanced hybridization gap [74–76].

Having analyzed the effects of IECs on the electronic structure, we below investigate how they affect superconductivity. In light of the reported signatures of a spin density wave (SDW) in $La_3Ni_2O_7$ at ambient pressure [37,38,77–82], it may be natural to consider spin-fluctuation-mediated pairing.

A phase transition to the superconducting state occurs when the corresponding pairing susceptibility diverges, which requires numerical evaluation of the pairing vertex $\mathbf{\Gamma}^{\mathrm{s/t}}$ for singlet (s) or triplet (t) Cooper pairs [39,40] (bold symbols will be used to denote vectors and matrices). The spin and charge susceptibilities ($\boldsymbol{\chi}^{\mathrm{sp/ch}}$) and the related irreducible vertices ($\mathbf{\Gamma}^{\mathrm{sp/ch}}$) contribute to $\mathbf{\Gamma}^{\mathrm{s/t}}$. Calculating frequency- and momentum-dependent $\mathbf{\Gamma}^{\mathrm{sp/ch}}$ and $\boldsymbol{\chi}^{\mathrm{sp/ch}}$, however, is highly nontrivial for multiorbital systems. We thus follow an idea previously employed to study cuprates, ruthenates, and iron-based superconductors [41–44]. Namely, $\mathbf{\Gamma}^{\mathrm{sp/ch}}$ are parametrized by effective intraorbital Coulomb interaction $\bar{U}$ and Hund's coupling $\bar{J}$, i.e., $\mathbf{\Gamma}^{\mathrm{sp/ch}} \to \bar{\mathbf{\Gamma}}^{\mathrm{sp/ch}}(\bar{U}, \bar{J})$ (we assume the interorbital value $\bar{U}' = \bar{U} - 2\bar{J}$). The effective vertices $\bar{\mathbf{\Gamma}}^{\mathrm{sp/ch}}(\bar{U}, \bar{J})$ are independent of frequency and momentum, see Supplemental Material [35]. This leads to the gap equation

$$\lambda_{\mathrm{sc}}\Delta_{lm}(k) = -\frac{T}{2N}\sum_{q,l_1l_2m_1m_2}\Gamma^{\mathrm{s/t}}_{ll_1m_1m}(q) \times G_{l_1l_2}(k-q)G_{m_1m_2}(q-k)\Delta_{l_2m_2}(k-q), \quad (2)$$

where λ_{sc} is the eigenvalue, $G(k)$ the (C)DMFT Green's function, and $\Delta(k)$ the gap function. $k \equiv (\boldsymbol{k}, i\omega_n)$ and $q \equiv (\boldsymbol{q}, i\nu_n)$ with $\boldsymbol{k}$ and $\boldsymbol{q}$ being the crystal momentum and $\nu_n = 2n\pi/T$ the bosonic Matsubara frequency. N indicates the number of $\boldsymbol{k}$-points in the FBZ. $\Gamma^{\mathrm{s/t}}_{lm_1l_1m}(q = k - k')$ describe the particle-particle scattering of electrons in orbitals (l, m) with four-momenta $(k, -k)$ to (l_1, m_1) with $(k', -k')$. The transition to the superconducting state is indicated by the maximum eigenvalue λ_{sc} reaching unity. Since $\bar{\mathbf{\Gamma}}^{\mathrm{sp/ch}}(\bar{U}, \bar{J})$ are more sparse in the original e_g basis than the BA basis, so are the resulting $\boldsymbol{\chi}^{\mathrm{sp/ch}}$ and $\mathbf{\Gamma}^{\mathrm{s/t}}$. We therefore discuss $\boldsymbol{\chi}^{\mathrm{sp/ch}}$ and $\mathbf{\Gamma}^{\mathrm{s/t}}$ in the e_g picture.

We find the predominance of singlet over triplet pairings arising from antiferromagnetic (AFM) fluctuations. Figure 3(a) presents the resulting superconducting phase diagram for the leading singlet channel. Since we cannot pinpoint the precise magnitude of $\bar{U}$ and $\bar{J}$, we scan a range of values. The vertical axis is given by the Stoner enhancement factor α_{sp}, which indicates the maximum eigenvalue of $\bar{\mathbf{\Gamma}}^{\mathrm{sp}}(\bar{U}, \bar{J})\boldsymbol{\chi}^0(\boldsymbol{q}, i\nu_0)$ and gauges the proximity to a magnetic instability. Here, $\boldsymbol{\chi}^0$ is the irreducible susceptibility, $\chi^0_{lml'm'}(q) = -(T/N)\sum_k G_{ll'}(k+q)G_{m'm}(k)$, which is the lowest-order term of the spin susceptibility, $\boldsymbol{\chi}^{\mathrm{sp}} = \boldsymbol{\chi}^0[\mathbf{1} - \bar{\mathbf{\Gamma}}^{\mathrm{sp}}(\bar{U}, \bar{J})\boldsymbol{\chi}^0]^{-1}$. Thus, α_{sp} is determined entirely from $\bar{U}$ and $\bar{J}$, provided $\boldsymbol{\chi}^0(\boldsymbol{q}, i\nu_0)$ is given [35]. For both DMFT and CDMFT cases, the leading pairing symmetry in the e_g-orbital basis is always the intraorbital s-wave and interorbital $d_{x^2-y^2}$-wave pairing; see the inset of Fig. 3(a). Projecting to the noninteracting FS, this pairing corresponds to the $s\pm$ wave where the gap changes sign between the neighboring FS pockets [35]. This leading pairing symmetry is in line with many previous studies [8,12,13,18,21–23,25]. The qualitative features of the gap functions remain unchanged over the entire parameter range while $\boldsymbol{Q}$ [the crystal momentum at which the maximum eigenvalue of $\bar{\mathbf{\Gamma}}^{\mathrm{sp}}(\bar{U}, \bar{J})\boldsymbol{\chi}^0(\boldsymbol{q}, i\nu_0)$ emerges] changes from $\boldsymbol{Q} = (\pi, 0)$ for $\bar{J}/\bar{U} \lessapprox 0.06$ to an incommensurate wave vector around the M point for $\bar{J}/\bar{U} \gtrapprox 0.06$ for both DMFT and CDMFT as highlighted in Fig. 3(b); see Supplemental Material for the details [35].

The most notable feature of the phase diagram presented in Fig. 3(a) is the enhanced superconducting instabilities in CDMFT compared to DMFT. This result is quite surprising

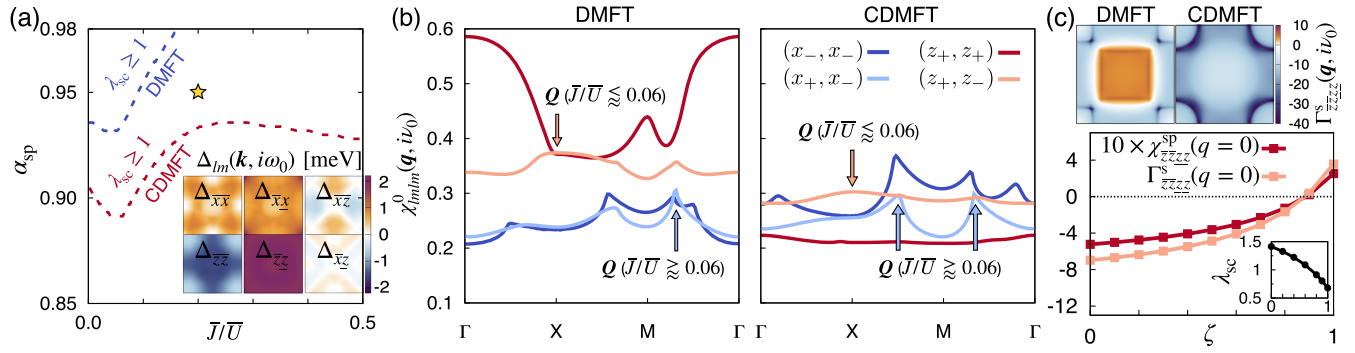

FIG. 3. (a) Superconducting phase diagram in the α_{sp}–$\bar{J}/\bar{U}$ space at $T = 1/145$ eV $\simeq 80$ K. The superconductivity sets in (i.e., $\lambda_{sc} \geq 1$) in the regions above the dashed lines; blue for the DMFT and red for the CDMFT. Inset: the CDMFT gap functions in the FBZ for the parameter set marked by the yellow star which corresponds to $\alpha_{sp} = 0.95$ and $\bar{J}/\bar{U} = 0.2$. (b) The irreducible susceptibilities at the lowest bosonic frequency $\chi^0_{lmlm}(\boldsymbol{q}, i\nu_0)$ calculated using DMFT (left) and CDMFT (right) Green's functions. $\boldsymbol{Q}$ and the associated $\boldsymbol{\chi}^0(\boldsymbol{q}, i\nu_0)$ components are highlighted with colored arrows. (c) Upper panel: the spin-singlet pairing interaction $\Gamma^s_{\bar{z}\bar{z}\underline{z}\underline{z}}(\boldsymbol{q}, i\nu_0)$ between top and bottom layer z orbitals in the FBZ. Lower panel: $\chi^{sp}_{\bar{z}\bar{z}\underline{z}\underline{z}}(q=0)$, $\Gamma^s_{\bar{z}\bar{z}\underline{z}\underline{z}}(q=0)$, and λ_{sc} (inset) as a function of scaling factor ζ for DMFT $\chi^0_{z_+z_+z_+z_+}(q)$. $\alpha_{sp} = 0.95$ and $\bar{J}/\bar{U} = 0.2$ for both panels.

because the γ pocket which disappears by IECs within our CDMFT calculation has been argued to drive the spin-fluctuation-mediated superconductivity throughout the literature [9,13,16,18,21]. It thus raises the question: What is the role of the γ pocket in the pairing?

We first find that the γ pocket has a "Janus-faced" role: It hosts both obstructive and supportive magnetic fluctuations for the singlet pairing. This can be, in fact, traced back to the behavior of $\chi^0_{lmlm}(\boldsymbol{q}, i\nu_0)$ by investigating the $(l, m) = (z_+, z_+)$ and (z_+, z_-) components of the DMFT calculation in Fig. 3(b). While the γ pocket allows for small-$\boldsymbol{q}$ particle-hole excitations resulting in the $\boldsymbol{q} = (0, 0)$ interlayer FM $\chi^0_{z_+z_+z_+z_+}(\boldsymbol{q}, i\nu_0)$, the $\boldsymbol{q} = (\pi, 0)$ nesting between the γ and β pocket gives rise to AFM $\chi^0_{z_+z_-z_+z_-}(\boldsymbol{q}, i\nu_0)$. Thus, the γ pocket promotes two different competing (i.e., FM vs AFM) magnetic channels. Importantly, however, the FM $\chi^0_{z_+z_+z_+z_+}(\boldsymbol{q}, i\nu_0)$ predominates in DMFT as clearly shown in the left panel of Fig. 3(b).

The disappearance of the γ pocket from the FS due to IECs within CDMFT results in the suppression of both channels, especially the $\chi^0_{z_+z_+z_+z_+}$ component involving solely the γ pocket [Fig. 3(b)]. This change is more apparent from the sign of the pairing interaction. In the singlet channel, the FM fluctuation is directly manifested by a repulsive (rather than attractive) interaction $\Gamma^s_{\bar{z}\bar{z}\underline{z}\underline{z}}(q = 0)$ [upper panel of Fig. 3(c)], which hinders the singlet Cooper pairing between $\bar{z}$ and $\underline{z}$ orbitals. Quenching of the FM $\chi^0_{z_+z_+z_+z_+}$ as in CDMFT yields the attractive pairing interaction $\Gamma^s_{\bar{z}\bar{z}\underline{z}\underline{z}}$ over the entire FBZ; see Fig. 3(c). Hence, the enhanced pairing tendency in CDMFT is mainly attributed to the suppression of this FM channel upon undergoing the Lifshitz transition.

To further corroborate this argument, we analyze how the DMFT superconducting instabilities are affected by the FM fluctuation by introducing a scaling factor ζ for $\chi^0_{z_+z_+z_+z_+}(q)$. Namely, $\chi^0_{z_+z_+z_+z_+}(q)$ is rescaled to $\zeta\chi^0_{z_+z_+z_+z_+}(q)$ before constructing $\boldsymbol{\chi}^{sp/ch}$ and $\boldsymbol{\Gamma}^s$. Indeed, as shown in the lower panel of Fig. 3(c), the interlayer FM spin susceptibility $\chi^{sp}_{\bar{z}\bar{z}\underline{z}\underline{z}}(q = 0)$ turns AFM with decreasing ζ followed by an attractive pairing interaction $\Gamma^s_{\bar{z}\bar{z}\underline{z}\underline{z}}(q = 0)$ and an increase of λ_{sc}. See Supplemental Material for additional data [35]. Note also that since the γ pocket is the only FS pocket dispersive along the k_z direction [19], the disappearance of the γ pocket by IECs makes $La_3Ni_2O_7$ effectively two dimensional.

We now turn to the question of "Why does superconductivity emerge only in the high-pressure phase?" A useful insight is obtained from a recent experiment which reports that pressure mainly shrinks the out-of-plane Ni—O bond length while the in-plane one is weakly affected [45]. Thus, the main effect of pressure can be addressed with the change of $t^z_\perp$ which is sensitive to the out-of-plane Ni-O bond length. Since $t^z_\perp \simeq -0.63$ eV at 29.5 GPa under which superconductivity emerges [6,8,13], a smaller magnitude of $t^z_\perp$ should correspond to the lower pressure case. In light of this observation, we investigate two "low pressure" cases, namely, $t^z_\perp = -0.45$ and $t^z_\perp = -0.55$ eV, using CDMFT.

In Fig. 4(a), we find that large $\chi^0_{z_+z_+z_+z_+}(\boldsymbol{q}, i\nu_0)$ emerges for the two low-pressure cases, in sharp contrast to the high-pressure result ($t^z_\perp \simeq -0.63$ eV), which we have already noticed in Fig. 3. Interestingly, this result provides a plausible scenario of why $La_3Ni_2O_7$ is not superconducting in the low-pressure phase because FM $\chi^0_{z_+z_+z_+z_+}(\boldsymbol{q}, i\nu_0)$ obstructs the singlet pairing as detailed above. While the γ pocket gives rise to strong FM fluctuations, the actual magnetic transition occurs at a finite $\boldsymbol{q}$ as shown in Fig. 4(b) which presents the maximum eigenvalue of the spin susceptibility at each $\boldsymbol{q}$, $\chi^{sp}_{max}(\boldsymbol{q}, i\nu_0)$, for $t^z_\perp = -0.45$ eV. $\chi^{sp}_{max}(\boldsymbol{q}, i\nu_0)$ shows a peak at $\boldsymbol{q} = \boldsymbol{Q}_{SDW}$ which is different

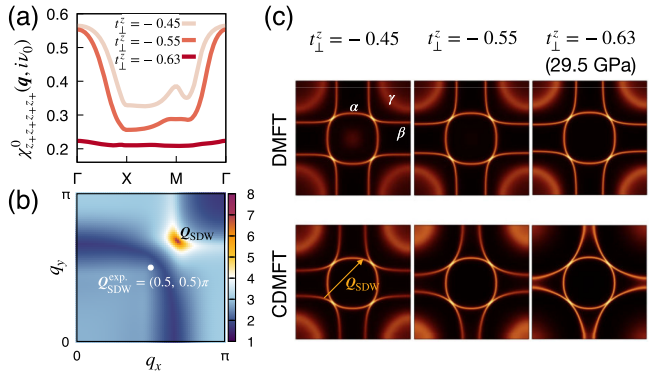

FIG. 4. (a) $\chi^0_{z_+z_+z_+z_+}(\boldsymbol{q}, i\nu_0)$ calculated using CDMFT Green's functions for three different values of $t_\perp^z$ (in units of eV). (b) $\chi^{sp}_{max}(\boldsymbol{q}, i\nu_0)$ at $\alpha_{sp} = 0.95$ and $\bar{J}/\bar{U} = 0.2$ for $t_\perp^z = -0.45$ eV. (c) FSs obtained from DMFT and CDMFT for the same values of $t_\perp^z$. We used $U = 3.7$, $J = 0.6$ eV, and $U' = U - 2J$ for all the cases. $\boldsymbol{Q}_{SDW}$ in (b) is highlighted with the orange arrow.

from but close to the SDW wave vector $\boldsymbol{Q}^{exp}_{SDW} = (0.5, 0.5)\pi$ reported by experiments [37,38]. See Supplemental Material for further discussion [35].

To trace the origin of the difference between the two low-pressure cases and the high-pressure ($t_\perp^z \simeq -0.63$ eV) case, we investigate the CDMFT FSs [lower panels in Fig. 4(c)]. The strength of IECs is controlled by $|t_\perp^z|$, so the shape of the β and the γ pockets in CDMFT FS is basically the same as the DMFT FS for the smallest $|t_\perp^z|$ ($t_\perp^z = -0.45$ eV). As $|t_\perp^z|$ increases, however, the γ pocket gets suppressed in CDMFT which is consistent with the evolution of $\chi^0_{z_+z_+z_+z_+}(\boldsymbol{q}, i\nu_0)$ presented in Fig. 4(a); see Supplemental Material for further discussion on the microscopic origin, especially on the change of the β pocket [35]. At $t_\perp^z \simeq -0.63$ eV, the FS that we have already seen in Fig. 2(b) is realized. In contrast, the FS is almost unaffected by $t_\perp^z$ in DMFT. Hence, it can be seen that the concerted effect of pressure (as modeled via $t_\perp^z$) and IECs induces the Lifshitz transition. This transition quenches the FM channel resulting in an enhancement of the singlet pairing mediated by AFM fluctuations.

We finally discuss implications of the above pressure-induced FS change for the available experimental data. Since the SDW is known to emerge in the ambient-pressure phase [37,38,77–82], direct comparison of our FS for small $|t_\perp^z|$ with experimental FS obtained from angle-resolved photoemission spectroscopy under ambient pressure [46] may be misleading. Also, considering that there is a discrepancy as to whether or not the γ pocket crosses the Fermi level in $La_4Ni_3O_{10}$ even between experiments [47,48], the same issue may also pertain to $La_3Ni_2O_7$. Further study is required. Rather, a tantalizing signature of the Lifshitz transition of FS is seen in the pressure dependence of Hall coefficient (R_H) [3,83]. While the sign of R_H is positive for the entire pressure range, a drop of R_H occurs near ∼10 GPa followed by the emergence of superconductivity [3,83]. Since the γ pocket is a holelike FS [Fig. 2(d)] and is destructive for pairing, the drop of R_H and the emergence of superconductivity is quite naturally explained from our Lifshitz transition scenario.

To conclude, we have demonstrated that IECs play a critical role in $La_3Ni_2O_7$ by inducing a Lifshitz transition. The superconducting instability is found to be enhanced by this transition due to the quenching of the FM fluctuation, which may also explain why superconductivity emerges only under high pressure.

Acknowledgments—We are grateful to F. Lechermann and I. Eremin for useful discussion. S. R. thanks Se Young Park for helpful comments on the charge self-consistency. This work is supported by the Cluster of Excellence "CUI: Advanced Imaging of Matter" of the Deutsche Forschungsgemeinschaft (DFG)—EXC 2056—project ID 390715994, by DFG priority program SPP 2244 (WE 5342/5-1 Project No. 422707584) and the DFG research unit FOR 5242 (WE 5342/7-1, Project No. 449119662). Calculations were done on the supercomputer Lise at NHR@ZIB as part of the NHR infrastructure under the project hhp00056.

[1] H. Sun, M. Huo, X. Hu, J. Li, Z. Liu, Y. Han, L. Tang, Z. Mao, P. Yang, B. Wang, J. Cheng, D.-X. Yao, G.-M. Zhang, and M. Wang, Nature (London) **621**, 493 (2023).
[2] J. Hou, P.-T. Yang, Z.-Y. Liu, J.-Y. Li, P.-F. Shan, L. Ma, G. Wang, N.-N. Wang, H.-Z. Guo, J.-P. Sun, Y. Uwatoko, M. Wang, G.-M. Zhang, B.-S. Wang, and J.-G. Cheng, Chin. Phys. Lett. **40**, 117302 (2023).
[3] Y. Zhang, D. Su, Y. Huang, H. Sun, M. Huo, Z. Shan, K. Ye, Z. Yang, R. Li, M. Smidman, M. Wang, L. Jiao, and H. Yuan, Nat. Phys. **20**, 1269 (2024).
[4] G. Wang, N. N. Wang, X. L. Shen, J. Hou, L. Ma, L. F. Shi, Z. A. Ren, Y. D. Gu, H. M. Ma, P. T. Yang, Z. Y. Liu, H. Z. Guo, J. P. Sun, G. M. Zhang, S. Calder, J.-Q. Yan, B. S. Wang, Y. Uwatoko, and J.-G. Cheng, Phys. Rev. X **14**, 011040 (2024).
[5] M. Zhang, C. Pei, Q. Wang, Y. Zhao, C. Li, W. Cao, S. Zhu, J. Wu, and Y. Qi, J. Mater. Sci. Technol. **185**, 147 (2024).
[6] Z. Luo, X. Hu, M. Wang, W. Wú, and D.-X. Yao, Phys. Rev. Lett. **131**, 126001 (2023).
[7] D. A. Shilenko and I. V. Leonov, Phys. Rev. B **108**, 125105 (2023).
[8] Y. Gu, C. Le, Z. Yang, X. Wu, and J. Hu, arXiv:2306.07275.
[9] F. Lechermann, J. Gondolf, S. Bötzel, and I. M. Eremin, Phys. Rev. B **108**, L201121 (2023).
[10] Y. Zhang, L.-F. Lin, A. Moreo, and E. Dagotto, Phys. Rev. B **108**, L180510 (2023).
[11] Y. Cao and Y. F. Yang, Phys. Rev. B **109**, L081105 (2024).
[12] Q.-G. Yang, D. Wang, and Q.-H. Wang, Phys. Rev. B **108**, L140505 (2023).
[13] H. Sakakibara, N. Kitamine, M. Ochi, and K. Kuroki, Phys. Rev. Lett. **132**, 106002 (2024).

[14] R. Jiang, J. Hou, Z. Fan, Z.-J. Lang, and W. Ku, Phys. Rev. Lett. **132**, 126503 (2024).
[15] L. C. Rhodes and P. Wahl, Phys. Rev. Mater. **8**, 044801 (2024).
[16] Y. Zhang, L.-F. Lin, A. Moreo, T. A. Maier, and E. Dagotto, Phys. Rev. B **108**, 165141 (2023).
[17] B. Geisler, J. J. Hamlin, G. R. Stewart, R. G. Hennig, and P. J. Hirschfeld, npj Quantum Mater. **9**, 38 (2024).
[18] Y.-B. Liu, J.-W. Mei, F. Ye, W.-Q. Chen, and F. Yang, Phys. Rev. Lett. **131**, 236002 (2023).
[19] H. LaBollita, V. Pardo, M. R. Norman, and A. S. Botana, arXiv:2309.17279.
[20] H. Sakakibara, M. Ochi, H. Nagata, Y. Ueki, H. Sakurai, R. Matsumoto, K. Terashima, K. Hirose, H. Ohta, M. Kato, Y. Takano, and K. Kuroki, Phys. Rev. B **109**, 144511 (2024).
[21] Y. Zhang, L.-F. Lin, A. Moreo, T. A. Maier, and E. Dagotto, Nat. Commun. **15**, 2470 (2024).
[22] H. Oh and Y.-H. Zhang, Phys. Rev. B **108**, 174511 (2023).
[23] Z. Liao, L. Chen, G. Duan, Y. Wang, C. Liu, R. Yu, and Q. Si, Phys. Rev. B **108**, 214522 (2023).
[24] Q. Qin and Y. F. Yang, Phys. Rev. B **108**, L140504 (2023).
[25] C. Lu, Z. Pan, F. Yang, and C. Wu, Phys. Rev. Lett. **132**, 146002 (2024).
[26] Y.-H. Tian, Y. Chen, J.-M. Wang, R.-Q. He, and Z.-Y. Lu, Phys. Rev. B **109**, 165154 (2024).
[27] D.-C. Lu, M. Li, Z.-Y. Zeng, W. Hou, J. Wang, F. Yang, and Y.-Z. You, arXiv:2308.11195.
[28] H. Lange, L. Homeier, E. Demler, U. Schollwöck, F. Grusdt, and A. Bohrdt, arXiv:2309.15843.
[29] W. Wú, Z. Luo, D.-X. Yao, and M. Wang, Sci. China Phys. Mech. Astron. **67**, 117402 (2024).
[30] K. Momma and F. Izumi, J. Appl. Crystallogr. **44**, 1272 (2011).
[31] A. I. Lichtenstein and M. I. Katsnelson, Phys. Rev. B **62**, R9283 (2000).
[32] G. Kotliar, S. Y. Savrasov, G. Pálsson, and G. Biroli, Phys. Rev. Lett. **87**, 186401 (2001).
[33] T. A. Maier, M. Jarrell, T. Pruschke, and M. Hettler, Rev. Mod. Phys. **77**, 1027 (2005).
[34] V. Christiansson, F. Petocchi, and P. Werner, Phys. Rev. Lett. **131**, 206501 (2023).
[35] See Supplemental Material at http://link.aps.org/supplemental/10.1103/PhysRevLett.133.096002 for additional data and discussion, which includes Refs. [1,6–11,13,16–19,21,34,36–69].
[36] E. Gull, A. J. Millis, A. I. Lichtenstein, A. N. Rubtsov, M. Troyer, and P. Werner, Rev. Mod. Phys. **83**, 349 (2011).
[37] Z. Dan, Y. Zhou, M. Huo, Y. Wang, L. Nie, M. Wang, T. Wu, and X. Chen, arXiv:2402.03952.
[38] X. Chen, J. Choi, Z. Jiang, J. Mei, K. Jiang, J. Li, S. Agrestini, M. Garcia-Fernandez, X. Huang, H. Sun, D. Shen, M. Wang, J. Hu, Y. Lu, K.-J. Zhou, and D. Feng, arXiv:2401.12657.
[39] N. E. Bickers, in *Theoretical Methods for Strongly Correlated Electrons*, CRM Series in Mathematical Physics, edited by D. Sénéchal, A.-M. Tremblay, and C. Bourbonnais (Springer, New York, NY, 2004), pp. 237–296.
[40] G. Rohringer, H. Hafermann, A. Toschi, A. A. Katanin, A. E. Antipov, M. I. Katsnelson, A. I. Lichtenstein, A. N. Rubtsov, and K. Held, Rev. Mod. Phys. **90**, 025003 (2018).
[41] T. A. Maier, M. Jarrell, and D. J. Scalapino, Phys. Rev. B **75**, 134519 (2007).
[42] R. Nourafkan, G. Kotliar, and A. M. S. Tremblay, Phys. Rev. Lett. **117**, 137001 (2016).
[43] O. Gingras, R. Nourafkan, A.-M. S. Tremblay, and M. Côté, Phys. Rev. Lett. **123**, 217005 (2019).
[44] S. Käser, H. U. R. Strand, N. Wentzell, A. Georges, O. Parcollet, and P. Hansmann, Phys. Rev. B **105**, 155101 (2022).
[45] L. Wang, Y. Li, S. Xie, F. Liu, H. Sun, C. Huang, Y. Gao, T. Nakagawa, B. Fu, B. Dong, Z. Cao, R. Yu, S. I. Kawaguchi, H. Kadobayashi, M. Wang, C. Jin, H. kwang Mao, and H. Liu, arXiv:2311.09186.
[46] J. Yang *et al.*, Nat. Commun. **15**, 4373 (2024).
[47] H. Li, X. Zhou, T. Nummy, J. Zhang, V. Pardo, W. E. Pickett, J. F. Mitchell, and D. S. Dessau, Nat. Commun. **8**, 704 (2017).
[48] X. Du, Y. D. Li, Y. T. Cao, C. Y. Pei, M. X. Zhang, W. X. Zhao, K. Y. Zhai, R. Z. Xu, Z. K. Liu, Z. W. Li, J. K. Zhao, G. Li, Y. L. Chen, Y. P. Qi, H. J. Guo, and L. X. Yang, arXiv:2405.19853.
[49] Z. Liu, M. Huo, J. Li, Q. Li, Y. Liu, Y. Dai, X. Zhou, J. Hao, Y. Lu, M. Wang, and H.-H. Wen, arXiv:2307.02950.
[50] J. Mravlje, M. Aichhorn, T. Miyake, K. Haule, G. Kotliar, and A. Georges, Phys. Rev. Lett. **106**, 096401 (2011).
[51] S. Ryee, M. J. Han, and S. Choi, Phys. Rev. Lett. **126**, 206401 (2021).
[52] S. Ryee, S. Choi, and M. J. Han, Phys. Rev. Res. **5**, 033134 (2023).
[53] T. Ayral, S. Biermann, and P. Werner, Phys. Rev. B **87**, 125149 (2013).
[54] M. Schüler, M. Rösner, T. O. Wehling, A. I. Lichtenstein, and M. I. Katsnelson, Phys. Rev. Lett. **111**, 036601 (2013).
[55] E. G. C. P. van Loon, M. Schüler, M. I. Katsnelson, and T. O. Wehling, Phys. Rev. B **94**, 165141 (2016).
[56] F. Nilsson, L. Boehnke, P. Werner, and F. Aryasetiawan, Phys. Rev. Mater. **1**, 043803 (2017).
[57] S. Ryee, P. Sémon, M. J. Han, and S. Choi, npj Quantum Mater. **5**, 19 (2020).
[58] A. H. Nevidomskyy and P. Coleman, Phys. Rev. Lett. **103**, 147205 (2009).
[59] Z. P. Yin, K. Haule, and G. Kotliar, Phys. Rev. B **86**, 195141 (2012).
[60] A. Georges, L. d. Medici, and J. Mravlje, Annu. Rev. Condens. Matter Phys. **4**, 137 (2013).
[61] C. Aron and G. Kotliar, Phys. Rev. B **91**, 041110(R) (2015).
[62] S. Ryee and T. O. Wehling, Nano Lett. **23**, 573 (2023).
[63] J. Li, M. Wallerberger, N. Chikano, C.-N. Yeh, E. Gull, and H. Shinaoka, Phys. Rev. B **101**, 035144 (2020).
[64] N. Witt, E. G. C. P. van Loon, T. Nomoto, R. Arita, and T. O. Wehling, Phys. Rev. B **103**, 205148 (2021).
[65] N. Witt, J. M. Pizarro, J. Berges, T. Nomoto, R. Arita, and T. O. Wehling, Phys. Rev. B **105**, L241109 (2022).
[66] N. Witt, L. Si, J. M. Tomczak, K. Held, and T. O. Wehling, SciPost Phys. **15**, 197 (2023).
[67] H. Shinaoka, J. Otsuki, M. Ohzeki, and K. Yoshimi, Phys. Rev. B **96**, 035147 (2017).
[68] H. Shinaoka, N. Chikano, E. Gull, J. Li, T. Nomoto, J. Otsuki, M. Wallerberger, T. Wang, and K. Yoshimi, SciPost Phys. Lect. Notes 63 (2022).

[69] M. Wallerberger, S. Badr, S. Hoshino, S. Huber, F. Kakizawa, T. Koretsune, Y. Nagai, K. Nogaki, T. Nomoto, H. Mori, J. Otsuki, S. Ozaki, T. Plaikner, R. Sakurai, C. Vogel, N. Witt, K. Yoshimi, and H. Shinaoka, SoftwareX **21**, 101266 (2023).
[70] C. Melnick, P. Sémon, K. Yu, N. D'Imperio, A.-M. Tremblay, and G. Kotliar, Comput. Phys. Commun. **267**, 108075 (2021).
[71] A. Georges, G. Kotliar, W. Krauth, and M. J. Rozenberg, Rev. Mod. Phys. **68**, 13 (1996).
[72] M. Jarrell and J. Gubernatis, Phys. Rep. **269**, 133 (1996).
[73] D. Bergeron and A.-M. S. Tremblay, Phys. Rev. E **94**, 023303 (2016).
[74] S. Biermann, A. Poteryaev, A. I. Lichtenstein, and A. Georges, Phys. Rev. Lett. **94**, 026404 (2005).
[75] J. M. Tomczak, F. Aryasetiawan, and S. Biermann, Phys. Rev. B **78**, 115103 (2008).
[76] W. H. Brito, M. C. O. Aguiar, K. Haule, and G. Kotliar, Phys. Rev. Lett. **117**, 056402 (2016).
[77] Z. Zhang, M. Greenblatt, and J. B. Goodenough, J. Solid State Chem. **108**, 402 (1994).
[78] S. Taniguchi, T. Nishikawa, Y. Yasui, Y. Kobayashi, J. Takeda, S.-i. Shamoto, and M. Sato, J. Phys. Soc. Jpn. **64**, 1644 (1995).
[79] G. Wu, J. J. Neumeier, and M. F. Hundley, Phys. Rev. B **63**, 245120 (2001).
[80] C. D. Ling, D. N. Argyriou, G. Wu, and J. J. Neumeier, J. Solid State Chem. **152**, 517 (2000).
[81] Z. Liu, H. Sun, M. Huo, X. Ma, Y. Ji, E. Yi, L. Li, H. Liu, J. Yu, Z. Zhang, Z. Chen, F. Liang, H. Dong, H. Guo, D. Zhong, B. Shen, S. Li, and M. Wang, Sci. China Phys. Mech. Astron. **66**, 217411 (2022).
[82] K. Chen, X. Liu, J. Jiao, M. Zou, C. Jiang, X. Li, Y. Luo, Q. Wu, N. Zhang, Y. Guo, and L. Shu, Phys. Rev. Lett. **132**, 256503 (2024).
[83] Y. Zhou, J. Guo, S. Cai, H. Sun, P. Wang, J. Zhao, J. Han, X. Chen, Q. Wu, Y. Ding, M. Wang, T. Xiang, H. kwang Mao, and L. Sun, arXiv:2311.12361.